Probing magnetostructural correlations in multiferroic $HoAl_3(BO_3)_4$

H. Zhang,[1] T. Yu,[1] Z. Chen,[2] C. S. Nelson,[3] L. N. Bezmaternykh,[4] A. M. M. Abeykoon,[3] and T. A. Tyson[1,*]

[1]*Department of Physics, New Jersey Institute of Technology, Newark, New Jersey 07102, USA*

[2]*Mineral Physics Institute, Stony Brook University, Stony Brook, New York 11794, USA*

[3]*Photon Science Division, Brookhaven National Laboratory, Upton, New York 11973, USA*

[4]*L.V. Kirensky Institute of Physics, Siberian Branch of RAS, Krasnoyarsk, 660036, Russia*

The system $HoAl_3(BO_3)_4$ has recently been found to exhibit a large magnetoelectric effect. To understand the mechanism, macroscopic and atomic level properties of $HoAl_3(BO_3)_4$ were explored by temperature and magnetic field dependent heat capacity measurements, pressure and temperature dependent x-ray diffraction measurements, as well as temperature and magnetic field dependent x-ray absorption fine structure measurements. The experimental work was complemented by density functional theory calculations. An anomalous change in the structure is found in the temperature range where large magnetoelectric effects occur. No significant structural change or distortion of the HoO_6 polyhedra is seen to occur with magnetic field. However, the magnetic field dependent structural measurements reveal enhanced correlation between neighboring HoO_6 polyhedra. This observed response is seen to saturate near 3 T. A qualitative atomic level description of the mechanism behind the large electric polarization induced by magnetic fields in the general class of $RAl_3(BO_3)_4$ systems (R = rare earth) is developed.

PACS number(s): 75.85.+t, 61.05.cf, 75.80.+q, 61.05.cj

I. INTRODUCTION

Multiferroics form a very diverse class of materials, and even today there is no universal "theory of multiferroics" that can describe them completely (see reviews in Ref. [1]). Obtaining a comprehensive picture of multiferroics requires detailed theoretical analysis and measurements on a broad class of specific systems. Generally, multiferroics can be divided into two classes. In one class, the coexisting magnetic and ferroelectric order parameters are weakly coupled, with the onset of ferroelectricity occurs independent of the appearance of magnetic ordering. In the other class of multiferroics, the magnetic ordering breaks the inversion symmetry and results in a polar state that supports ferroelectricity. Ferroelectricity can also be induced by charge ordering in multiferroics [2]. This coupling between magnetization and polarization typically occurs in systems with low net polarization (typically $< \sim 1 \,\mu C/Cm^2$). We note that the polarization value in most multiferroics is small compared to the classic ferroelectric systems such as $BaTiO_3$ ($P \sim 75 \,\mu C/cm^2$) [3].

In terms of applications, the most direct use for multiferroics is as magnetic field sensors utilizing the sensitivity of the electric polarization to magnetic fields [1,4]. Meanwhile, since multiferroics provide alternative ways to read and write data using both electric polarization and magnetization as well as the mutual control between them, multiferroics have a huge potential in data storage and memory devices [5]. Current industries favor the ferroelectric random access memory (FeRAM) devices despite the disadvantage of destructive read operation since magnetoresistive RAM (MRAM) devices are much slower and more power consuming during read/write operations. The availability of multiferroic materials with strong coupling between different ordered states will enable data storage systems with multiple components and devices

that can operate while using considerably less power than current devices. Other applications such as gate dielectrics for semiconductor devices [6] and piezoelectric transformer [7] were reported as well. Systematic experimental work has been conducted by many groups to enable these possible applications.

In the search for materials with larger magnetoelectric couplings, compounds including $Ni_3V_2O_8$ [8], $MnWO_4$ [9], $LiCu_2O_2$ [10], $CuFeO_2$ [11], $CoCr_2O_4$ [12], and other systems such as $Ba(Ti_{0.9}Fe_{0.1})O_{2.81}$ [13], $NdCrTiO_5$ [14], ferrites [15], and manganites [16] were examined. Interest in multiferroics was reignited by the discovery of strong coupling between magnetization and ferroelectricity in manganese based systems. For example, the rare earth manganites $RMnO_3$ [16] (R = rare earth, Y, In, and Sc) with hexagonal structure have a much higher ferroelectric transition temperature $Tc(\sim900 \text{ K})$ than the antiferromagnetic transition temperature $T_N(\sim70 \text{ K})$. On the other hand, a particularly appealing mechanism was identified in $TbMnO_3$ [16], in which ferroelectricity is induced by the formation of a symmetry-lowering magnetic ground state that lacks inversion symmetry. The resulting polarization is small ($\sim0.08 \,\mu C/cm^2$), but because it is caused directly by the magnetic ordering, a possible new magnetoelectric interaction should be expected. Orthorhombic RMn_2O_5 [16] (R = Tb, Dy, and Ho) was also found to exhibit significant magnetodielectric effects near a unique commensurate-incommensurate magnetic transition where magnetic transitions are intricately coupled with changes in the dielectric properties.

$BiFeO_3$, has received intense investigation because it is one of the few multiferroics with both ferroelectricity and magnetism occurring above room temperature, possibly enabling real devices (see reviews in Ref. [1]). In this system, Bi^{3+} ions with two electrons in a $6s$ orbit (lone pair) shift away from the centrosymmetric positions with respect to the surrounding oxygen ions, leading to ferroelectricity. Another interesting system is the magnetic oxide Ni_3TeO_6

*Corresponding author: tyson@njit.edu

[17]. Studies show that this system exhibits no signature of ferroelectricity down to 10 K (in zero magnetic field) but undergoes a single magnetic transition at 52 K, below which the system is antiferromagnetic. Recently, it was reported that this material exhibits nonhysteretic magnetoelectric switching at high magnetic fields. As another example, the $LuFe_2O_4$ [18] system is found to support ferroelectricity, which comes from the combination of two factors: crystal structure as well as the frustrated charge ordering. There is also a special compound family to be mentioned, which is the polar crystals with a strong interaction of the magnetic order parameter and the electrical polarization, such as $LiFeP_2O_7$ [19]. The coupling of the magnetic order parameter with the existing polarization makes it an interesting material to study.

One of the recently examined classes of multiferroic compounds is rare earth iron borates, $RFe_3(BO_3)_4$ ($R =$ rare earth, Y). These systems have attracted considerable attention mainly due to the noncentrosymmetric geometry and large magnetoelectric effects (with value of electric polarization of order $\sim 1\,\mu C/cm^2$), such as $GdFe_3(BO_3)_4$ [20], $DyFe_3(BO_3)_4$ [21], $HoFe_3(BO_3)_4$ [22], $YFe_3(BO_3)_4$ [22], $NdFe_3(BO_3)_4$ [23], and $PrFe_3(BO_3)_4$ [24]. Many interesting properties of this compound family have been discovered in recent years. For example, the study of $EuFe_3(BO_3)_4$ reveals the appearance of new phonon modes below 58 K [25] and changes in the phonon frequencies vs temperature plot near T_N giving evidence of spin–phonon coupling. The onset of the new phonon modes coincides with a structural transition from the $R32$ to the $P3_121$ space group on cooling. The appearance of new phonon modes is also reported in $PrFe_3(BO_3)_4$ at $\sim 30\,K$ [24]. This system is reported to have a strong coupling between the phonon and crystal-field excitations with coupling constant $W \sim 15\,cm^{-1}$. Meanwhile, studies have shown that the phonon frequencies change only weakly in $RFe_3(BO_3)_4$ for different R ions at room temperature [26]. We note that the $RFe_3(BO_3)_4$ system exhibit complex magnetic structure due to the presence for the magnetic R ($4f$) and Fe ($3d$) sites. The first magnetic transition (due to Fe ordering) occurs near $\sim 40\,K$. In the case for $R =$ Ho and Gd, spin reorientation of the Fe moments in the *a-b* plane occurs at lower temperatures $\sim 5\,K$ for Ho and $\sim 10\,K$ for Gd, due to strong coupling between spins on the R and Fe sites [20,22]. It has been found that the polarization along the *a* and *c* axes are related to the magnetic field induced ordering at the Fe and Ho sites, respectively. This behavior is not observed in the $R =$ Y, Er [27], and Tb systems [28].

Recent reports show that the transition metal Fe is not essential to establish large magnetoelectricity in this class of materials [29]. This suggests that a study of the properties of the isostructural compound $RAl_3(BO_3)_4$ ($RABO$), with only $4f$ electrons on the R site driving the magnetism, would be quite useful to determine the basic physics behind the borate systems. A first-principles calculation on $TbAl_3(BO_3)_4$ [30] revealed that this class of material has a very promising potential in magneto-optical usage. An experimental study of the $TmAl_3(BO_3)_4$ [29] system showed a magnetoelectric polarization reached values up to $0.03\,\mu C/cm^2$ at 7 T with the applied magnetic field along the *a* axis. The magneto-electric polarization is found to be proportional to the lattice contraction in magnetic field. The results of this investigation

clearly prove the existence of a significant coupling between the rare-earth magnetic moment and the lattice in $RAl_3(BO_3)_4$, although the atomic level description is not clear.

More recently a giant magnetoelectric effect of $P = 0.36\,\mu C/cm^2$ was found in $HoAl_3(BO_3)_4$ [31] along the *x* axis when a 7 T magnetic field is applied along the *y* axis. The magnetoelectric effect in the $HoAl_3(BO_3)_4$ system increased with decreasing magnetic anisotropy. This phenomenon is considered quite interesting because the value discovered is significantly higher than the reported values for other multiferroic compounds (for example, $TbMnO_3$ with $P = 0.08\,\mu C/cm^2$, $GdMn_2O_5$ with $P = 0.12\,\mu C/cm^2$). Meanwhile, although the measurement of magnetic susceptibility, magnetization, and polarization of the $RAl_3(BO_3)_4$ system has been conducted by other groups so far, the atomic level origin of magnetoelectric effect in the $HoAl_3(BO_3)_4$ system is still not yet understood. Microscopic models [32] of the $HoAl_3(BO_3)_4$ system have been developed and make definite predictions of the mechanism diving the ferroelectric coupling to polarization. A magnetostriction based mechanism involving distortion of the HoO_6 polyhedra with applied magnetic field was proposed.

To understand the microscopic level mechanism driving the coupling of electric polarization and magnetization in the $HoAl_3(BO_3)_4$ system, from a structural perspective a systematic study of the temperature dependent, pressure dependent, and magnetic field dependent structural properties was conducted. Measurements on multiple length scales were conducted. Both laboratory and synchrotron based measurements were carried out. The change in entropy was obtained by comparison of the simulated phonon contribution to the heat capacity and the measured total heat capacity (measured between 2 K and 300 K). Structural measurements under high pressure (up to $\sim 10\,GPa$) were conducted to probe the lattice stiffness and to access the low temperature behavior. Temperature dependent total scattering measurements (Bragg + diffuse scattering) were conducted between 10 K and 350 K to search for local distortions, which could support the magnetoelectric state. Magnetic field dependent local structural measurements (at 5 K for magnetic fields between 0 and 8 T) were conducted to search for details on the coupling of the atomic structure with the magnetic field. First-principles calculations of the density of state were conducted to assess the bands involved in the field induced magnetic polarization and to explore their level of spatial anisotropy (via the charge density).

II. EXPERIMENTAL AND COMPUTATIONAL METHODS

$HoAl_3(BO_3)_4$ single crystals were grown from solution melts based on bismuth trimolybdate and lithium molybdate. The preparation details can be found in Ref. [33]. The facets of the crystals are smooth. The color of crystals appears pink under fluorescent light. For all powder samples in experiments, the crystals were ground and sieved to 500 mesh particle size ($< 25\,\mu m$).

Single crystal diffraction measurements were conducted at room temperature on a single crystal of dimensions $0.19\,mm \times 0.30\,mm \times 0.58\,mm$ using an APEX II diffractometer with Cu Kα radiation following the experimental methods and

TABLE I. Structural parameters from single crystal refinement.[a]

Atoms	x		y		z	
Ho	0		0		0	
Al	0.8901(8)		2/3		2/3	
O1	0.8146(18)		0.4813(17)		0.83333	
O2	0.0770(22)		0.7436(22)		0.83333	
O3	0.8147(15)		0.7827(14)		0.8122(14)	
B1	2/3		1/3		0.83333	
B2	0.2210(28)		0.8870(28)		0.83333	
U_{ij} (Ho)	0.0074(13)	0.0074(13)	0.0112(15)	0.00372(63)	0.0000	0.0000
U_{ij} (Al)	0.0105(22)	0.0122(26)	0.0131(32)	0.0061(13)	0.0012(9)	0.0023(18)
U_{ij} (O1)	0.0244(57)	0.0244(57)	0.0055(56)	0.0167(70)	0.0040(27)	−0.0040(27)
U_{ij} (O2)	0.0152(70)	0.0152(70)	0.0041(70)	0.0050(68)	0.0015(34)	−0.0015(34)
U_{ij} (O3)	0.0210(58)	0.0204(6)	0.0117(43)	0.0098(51)	−0.0066(41)	−0.0002(43)
U_{ij} (B1)	0.0166(97)	0.0166(97)	0.0140(152)	0.0083(48)	0.0000	0.0000
U_{ij} (B2)	0.0108(77)	0.0108(77)	0.019(11)	−0.0005(104)	−0.0098(67)	0.0098(67)

Space Group: $R32$

$a = 9.2891(16)$ Å, $c = 7.2149(13)$ Å, $Dx = 4.445$ g/cm^3

Measurement temperature: 296 K

Crystal dimensions: $0.19 \times 0.30 \times 0.58$ mm^3

wavelength: 1.54178 Å,

2θ max: 143.5°

BASF twin parameter: 0.178(56)

Absorption coefficient: 25.25 mm^{-1}

EXTI extinction parameter: 0.01485(33)

Number of unique observed reflections Fo > $4\sigma(F_o)$: 228

Number of fitting parameters: 36

Amplitude of max peak in final difference map: 1.68 e/Å^3 (Al)

$R_1 = 4.98\%$, $wR_2 = 12.7\%$, Goodness of fit = 1.23

[a]Atomic displacement parameters U_{ij} (Å^2) are in the order U_{11}, U_{22}, U_{33}, U_{12}, U_{13}, and U_{23}.

analysis approach described in Ref. [34]. The structural refinement results are presented in Table I.

Heat capacity measurements on HoAl$_3$(BO$_3$)$_4$ single crystals were carried out with a Physical Property Measurement System (PPMS, Quantum Design) for magnetic fields up to 7 T on warming and cooling between 2 K and 300 K, utilizing a relaxation method [35]. Addenda measurements (grease without sample) were collected and subtracted from the sample measurements for each magnetic field.

For x-ray absorption fine structure (XAFS) measurements, polycrystalline samples were prepared by brushing the powder onto Kapton tape. Layers of tape were stacked to produce a uniform sample for transmission measurements with jump $\mu t \sim 1$, where $1/\mu$ is the absorption length. Spectra of HoAl$_3$(BO$_3$)$_4$ were measured at the National Synchrotron Light Source (NSLS) of Brookhaven National Laboratory (BNL) beamline X19A in ambient field vs temperature and at 5 K in a 10 T superconducting magnet for varying magnetic fields.

The density functional theory (DFT) based simulation of HoAl$_3$(BO$_3$)$_4$ was carried out by using the full-potential linearized augmented plane wave (FP-LAPW) method as implemented in the WIEN2k code [36]. The spin-polarized calculations with spin-orbit coupling (SOC) were conducted with the magnetization along the (001) direction. We used the local spin density approximation plus onsite Coulomb interaction (LSDA + U) method with $U_{eff} = 5$ eV. The crystal

structure of HoAl$_3$(BO$_3$)$_4$ was obtained from our single crystal x-ray diffraction measurement. The convergence parameter $R_{mt}K_{max}$ was set to 7 with $G_{max} = 18$. Two thousand uniformly distributed k-points were used. A total energy convergence of 10^{-5} Ry was used as the convergence criterion. The phonon density of states (DOS) was obtained by first optimizing the structure (coordinates) at the experimental lattice parameters and conducting a frozen phonon calculation using the VASP code [37]. The phonon DOS was then used to compute the heat capacity. The pressure dependent DFT calculations on the structure were also based on the VASP code.

High pressure x-ray diffraction experiments with powder samples were conducted on the X17C beamline at NSLS (at BNL). The data were collected in two independent runs for pressures between 0.6 to 10.2 GPa and for the range 2.0 to 9.0 GPa, respectively. Monochromatic focused beams of size 22 μm × 25 μm (first run) and 25 μm × 20 μm (second run) were used. A wavelength of 0.40660 Å was used for the first run and 0.40722Å was used for the second experiment. The powder diffraction images were collected with a Rayonix165 charge coupled device (CCD) detector. All experiments were performed in a diamond-anvil cell (DAC) with 400 μm culets with 4:1 methanol-ethanol mixture as the pressure transmitting medium. Several ruby chips were placed in different parts of the chamber for pressure measurements based on the ruby fluorescence wavelengths, and the average reading of three different rubies was used as the current

pressure. Two 4000-second scans were collected continuously for each pressure with the sample. The program Fit2D [38] was utilized to integrate the two-dimensional diffraction images to yield one-dimensional intensity vs 2θ XRD patterns. Rietveld refinements on the powder XRD data were conducted using the JANA2006 [39] software package.

Atomic pair distribution function (PDF) analysis [40] is an effective method of studying the structural information of materials incorporating both the periodic and disordered features. The relative atomic positions, or the interatomic positional correlations, can be described by the function $G(r) = 4\pi r[\rho(r) - \rho_0]$, where ρ_0 is the average atomic number density, $\rho(r)$ is the atomic pair density, and r is a radial distance from a given scattering center. We performed two independent x-ray powder diffraction experiments (Set A between 10 K and 350 K and Set B between 80 K and 350 K) to obtain the data required for the PDF study. Both were conducted at the X17A beamline at the NSLS, BNL. Data sets A and B both had the same experimental setup with x-ray beams $0.5 \, \text{mm} \times 0.5 \, \text{mm}$ in size and wavelength $\lambda = 0.1839 \, \text{Å}$. The sample was packed in a cylindrical polyimide capillary 1 mm in diameter. For data set A, it was placed 204.62 mm from the detector; for data set B it was placed 206.05 mm away. Calibrations were done by using a nickel standard. Set A was collected in a continuous flow cryostat with a cold finger, while set B was collected in a nitrogen gas stream system (Oxford Cryostream). The experimental background for each set-up was obtained by measuring empty sample holders in the same apparatus. The scattering data were collected with a Perkin-Elmer area detector. Multiple scans were performed for a total exposure time of 60 s (Set A) and 240 s (Set B) per temperature point. The Fit2D package was utilized to integrate two-dimensional diffraction images to yield one-dimensional intensity vs 2θ XRD patterns. The intensity data were corrected and normalized to obtain the total scattering structure function $S(Q)$ and then the atomic PDF, $G(r)$, using the PDFgetX3 [41] program. In the Fourier transform step to extract $G(r)$ from $S(Q)$, the limits for the Q range were chosen to reduce termination ripples. We used $Q_{\min} = 0.1 \, \text{Å}^{-1}$ and $Q_{\max} = 20.0 \, \text{Å}^{-1}$. The program PDFgui was used to refine the structure at each temperature based on the extracted $G(r)$ [42]. Data were first fit at 300 K (space group $R32$), and the refinement results were used for higher and lower temperature data sets for each consecutive temperature point. Unit cell parameters as well as atomic displacement parameters (ADPs) obtained from our single crystal x-ray measurement at room temperature were used as the initial values. In both data sets, anisotropic ADPs ($U_{11} = U_{22} \neq U_{33}$) were applied due to the hexagonal nature of the cell. The lattice parameters and ADPs were refined, but the atomic coordinates were held fixed. This latter assumption is expected to be appropriate in this extremely stiff material, as evidenced by the high pressure results. In addition, it provides the simplest model to track the temperature dependence.

III. RESULTS AND DISCUSSION

A. Crystal structure

Figure 1 shows the crystal structure of HoAl$_3$(BO$_3$)$_4$, and we note that the cell is hexagonal with space group $R32$. There
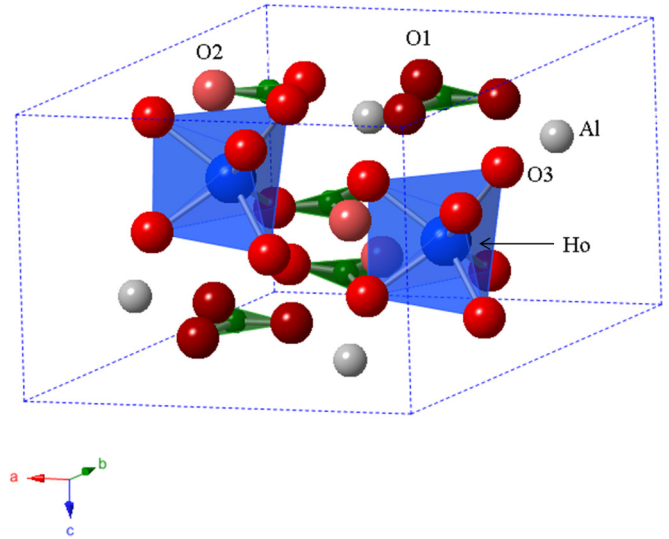

FIG. 1. (Color online) Crystal structure of hexagonal HoAl$_3$(BO$_3$)$_4$ with HoO$_6$ polyhedra connected by BO$_3$ planes containing O2 and O3 ions, while the BO$_3$ triangles with O1 ions are isolated.

are seven unique atomic positions in a unit cell: oxygen atoms occupy three different positions and boron atoms occupy two positions. We label them as O1, O2, O3 and B1, B2. Ho and Al atoms occupy separate unique sites. This labeling scheme will be used below. Ho^{3+} ions form HoO$_6$ polyhedra with six O3 atom first neighbors to the Ho site, in the shape of a slightly twisted prism. The HoO$_6$ polyhedra are connected with BO$_3$ triangles containing O2 and O3, while the BO$_3$ triangles containing only O1 are isolated from the HoO$_6$ polyhedra. No oxygen atom is shared by two nearby Ho ions. Tables I and II present the refinement results of single crystal x-ray diffraction data collected at the room temperature. The unit cell parameters presented in Table I are consistent with those of the materials in the RAl$_3$(BO$_3$)$_4$ family, like TbAl$_3$(BO$_3$)$_4$ [43]. ADPs are anisotropic ($U_{11} = U_{22} \neq U_{33}$) due to the hexagonal nature of the cell. Table II contains selected bond distances.

B. Heat capacity

There is no current experimental data available for the heat capacity of the RAl$_3$(BO$_3$)$_4$ family for comparison, while the behavior of the heat capacity from multiple materials in the RFe$_3$(BO$_3$)$_4$ system are well studied (see above). The heat capacity data collected in this paper for HoAl$_3$(BO$_3$)$_4$ are

TABLE II. Bond distances (Å).

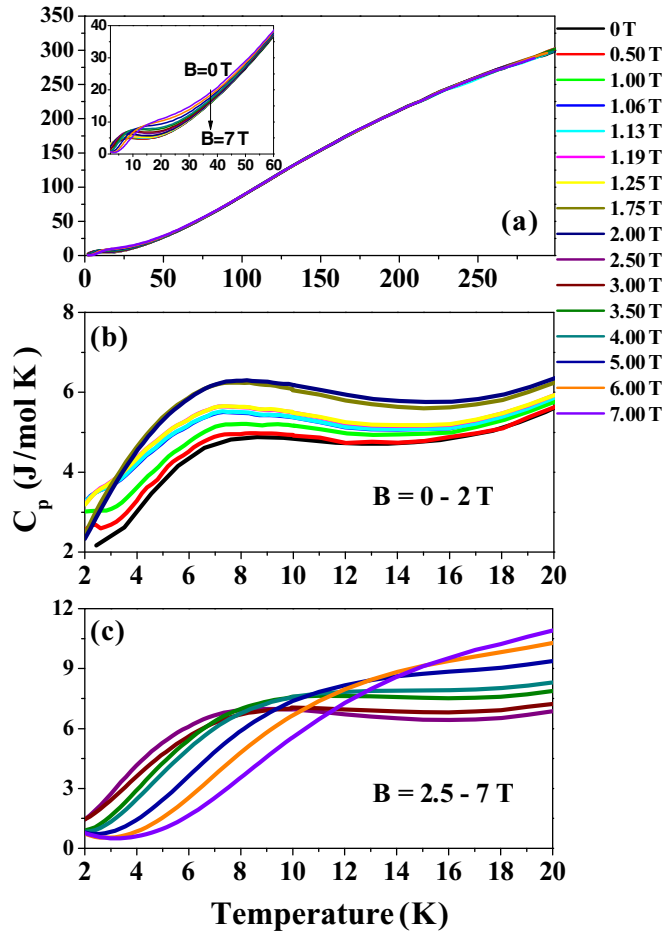| Bond Type	Distance
Ho-O3 $\times$ 6	2.323(11)
Al-O3 $\times$ 2	1.873(12)
Al-O1 $\times$ 2	1.923(11)
Al-O2 $\times$ 2	1.931(14)
B1-O1 $\times$ 3	1.374(17)
B2-O2	1.338(33)
B2-O3 $\times$ 2	1.367(17)

FIG. 2. (Color online) (a) Heat capacity measurement of HoAl$_3$(BO$_3$)$_4$ between 2 and 300 K under magnetic fields from 0 to 7 T. The inset shows the low temperature region between 2 and 60 K. (b), (c) Expanded scales for the region between 2 to 20 K. The position of the peak shifts to higher temperature for magnetic fields above 2 T.
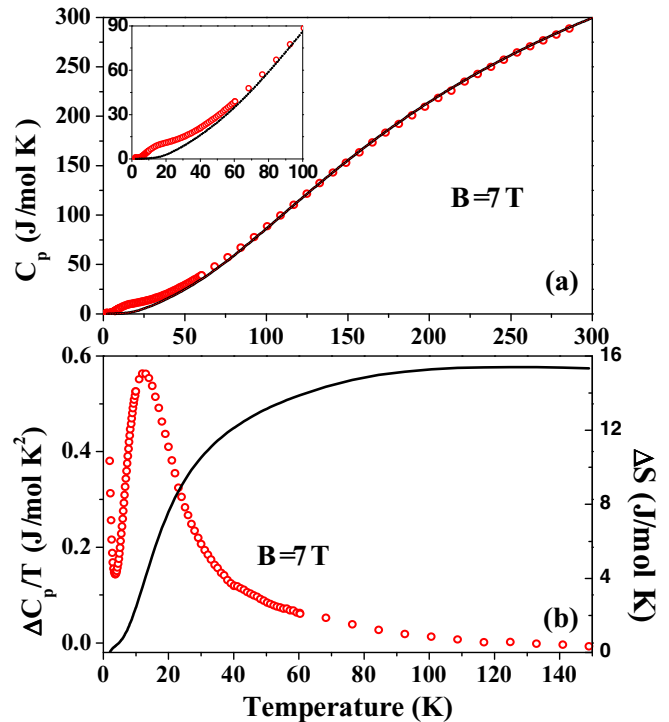

FIG. 3. (Color online) (a) Experimental value of heat capacity (red circles) at 7 T compared to the DFT simulated (modeling the phonons) result (black dashed line). The inset shows an expanded scale for the low temperature region. It can be seen that our simulated result agrees well with the experimental values in the high temperature region, while significant deviations starts to show up at around 60 K. (b) Difference of experimental and simulated value of heat capacity (red circles) between 0 and 150 K under 7 T and the calculated change in entropy (black solid line).

given in Figs. 2–4. Figures 2(a)–2(c) present the results of heat capacity measurements under variable temperatures (2–300 K) and magnetic fields (0–8 T). There is no structural phase transitions (sharp features) observed [Fig. 2(a)], although a smooth bump can be observed near 10 K [see the inset of Fig. 2(a)]. Measurements done on cooling from above this region down to 2 K and returning to the region above this feature (at 0 T) reveal no hysteresis, supporting the idea that there is no long range structural transition associated with this feature. The position of the feature near 10 K moves to higher temperatures for magnetic fields above 2 T. This feature is possibly associated with Schottky anomalies (associated with the Ho crystal field) or possibly with magnetic field induced ordering of Ho sites.

The contribution of the Ho subsystem in specific heat has been studied theoretically (Schottky) and calculated by Begunov *et al.*, based on a Hamiltonian, which includes crystal field, Zeeman, and Hyperfine interaction contributions [44]. Properties were calculated by diagonalizing the Hamiltonian for varying temperatures and magnetic fields. The contribution of the Ho subsystem was calculated by the formula $C_{\text{Ho}} =$

$k_B \frac{\langle E^2 \rangle - \langle E \rangle^2}{(k_B T)^2}$, where $\langle E^2 \rangle$ and $\langle E \rangle^2$ use the derived states for varying magnetic fields and temperatures. This atomiclike model predicted a shift of the wide peak near $\sim$10 K to the low temperature region for external magnetic fields between 0 to 1 T and towards the high temperature region for magnetic fields from 3 T to 6 T, which is similar to our results. Calculations were performed for magnetic fields at a limited set of values: 0, 0.1, 0.3, 0.5, 1, 3, and 6 T.

While the crystal field model has been used the describe the behavior of the heat capacity at low temperatures in the RAl$_3$(BO$_3$)$_4$ system, in RFe$_3$(BO$_3$)$_4$, evidence has been found for ordering at the R site for R = Nd, Sm, Er, Ho, and Tb. For R = Nd, both the Fe and Nd sites exhibit magnetic ordering below 30 K [45]. For the R = Sm system, simultaneous ordering of the Fe and Sm sites occurs at 34 K [46]. For R = Er, Tb, and Ho, ordering of both sites occurs at 32, 40 K, and 38 K, respectively [22,47]. In these systems, coupling between the Fe and R site occurs, which possibly enables this ordering. We note that recent work on the HoAl$_3$(BO$_3$)$_4$ system suggests ordering of the Ho site at a temperature that is consistent with the appearance of the magnetoelectric effect [48]. While both approaches have been applied to this system, the emphasis here is to understand the magnetostructural correlations.
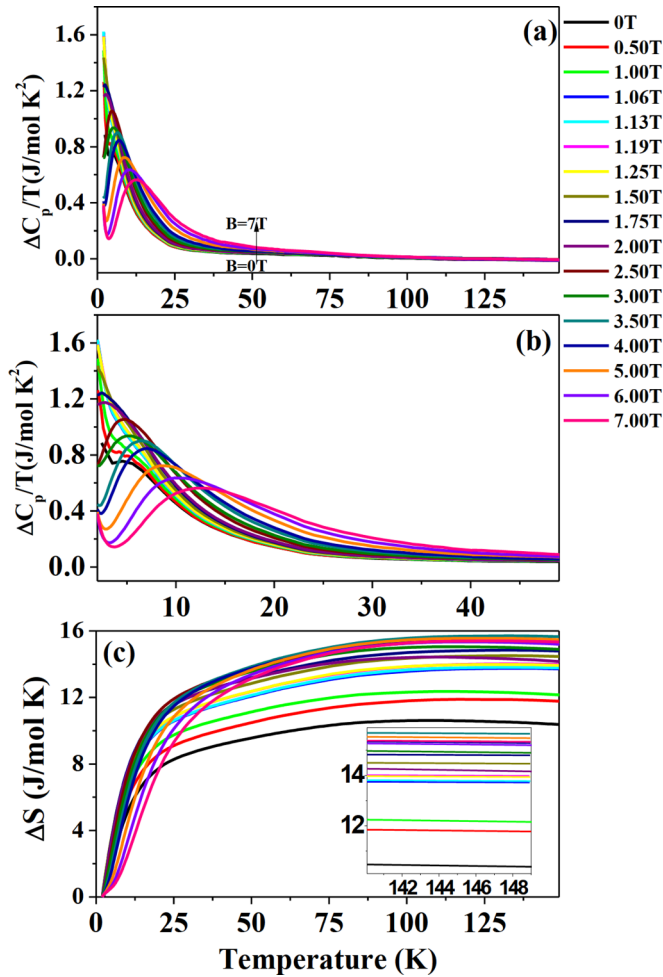
FIG. 4. (Color online) (a) Difference between the experimental and simulated value of heat capacity for magnetic fields from 0 to 7 T. (b) An expanded scale of temperature region between 2 and 50 K. The position of the peak shifts toward higher temperature region with the increasing magnetic field above 2 T, while no obvious trends are observed below 2 T. (c) The calculated changes in entropy. The curves converge to the same approximate value with increasing magnetic field. The inset is an expanded scale between 140 and 149 K.

It is found in this paper that the behavior of the specific heat has a strong magnetic field dependence. The black solid line in Fig. 3(a) gives our simulated result (DFT model of the phonons from the frozen phonon method) for the lattice-only contribution to the heat capacity of $HoAl_3(BO_3)_4$. The simulated and the experimental data match very well above $\sim$60 K. This suggests that the heat capacity of the HABO system is mostly from the lattice for temperatures above 60 K. The difference between the lattice and the measured heat capacity is indicated as ΔC_P, shown in Fig. 3(b) as the open circles. The change in entropy can be computed directly by integrating $\Delta C_P/T$. Figure 3(b) also shows the calculated change in entropy for a 7 T magnetic field. Figures 4(a)–4(c) give the overall picture of all of the data at all of the magnetic fields studied. The change in entropy is seen to approach a constant value with the increasing of temperature, as expected. It is seen to saturate for magnetic fields above $\sim$2 to 3 T. These results are consistent with the saturation
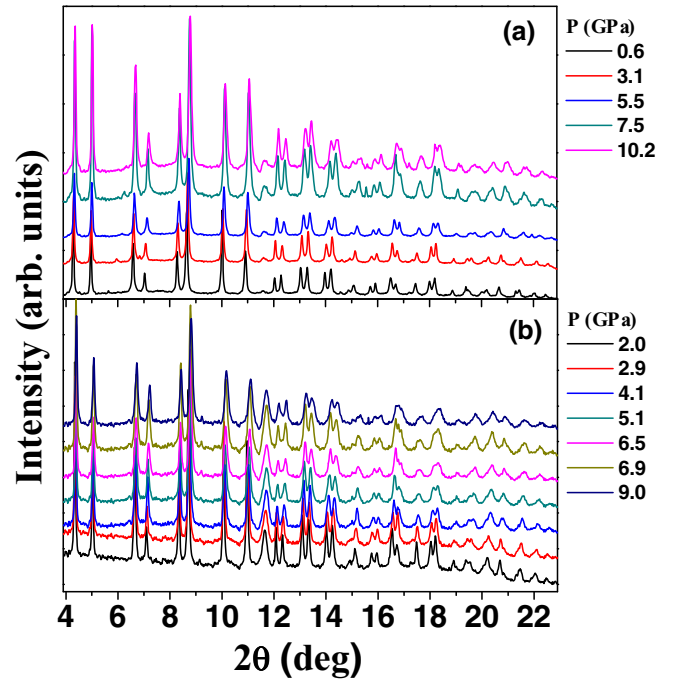

FIG. 5. (Color online) High pressure synchrotron XRD patterns of (a) set A, (b) set B for $HoAl_3(BO_3)_4$. Peak positions continue to shift systematically to higher 2θ values with increasing pressure.

of the magnetization for magnetic fields above $\sim$3 T [see Fig. 13(e)] at low temperature. However, it is important to note that our calculated results should be somewhat smaller than their actual values because of the omission of the region below 2 K in our measurements. This region is below the working range of our instrument. Both free Ho ion models and crystal field models predict saturation of the entropy with increasing magnetic fields. We note that in a single ion field induced Ho alignment model that the change in entropy has a value given by $\Delta S = R \ln(2S + 1)$. For Ho^{3+} $(4f^{10})$ with $S = 2$ (or $4\mu_B$ per Ho site), we obtain $\Delta S = 13.4$ J/(mol $\times$ K), which is close to observed results. To distinguish between these models, detailed crystal field modeling covering the range of magnetic fields and temperatures discussed here as well as systematic temperature and magnetic field dependent neutron diffraction experiments are needed. The models will be constrained by these heat capacity measurements. Here we focus on the magnetostructural properties.

C. High pressure x-ray diffraction

Figures 5–8 show the results from high-pressure x-ray diffraction measurements between 0.6 and 10.2 GPa. Figures 5(a) and 5(b) show the XRD patterns of $HoAl_3(BO_3)_4$ in two data sets. No new peak appears in the whole pressure range, indicating a continuous compression process on the samples without a structural phase change. The expected shift of the peaks to higher angle with increased pressure is seen. Rietveld refinements were performed on the XRD data to obtain the structural parameters. The profile of the refinement (data fit) is shown in Fig. 6 for $P = 0.64$ GPa. The small gasket peak region (steel gasket, indicated as *) was excluded during
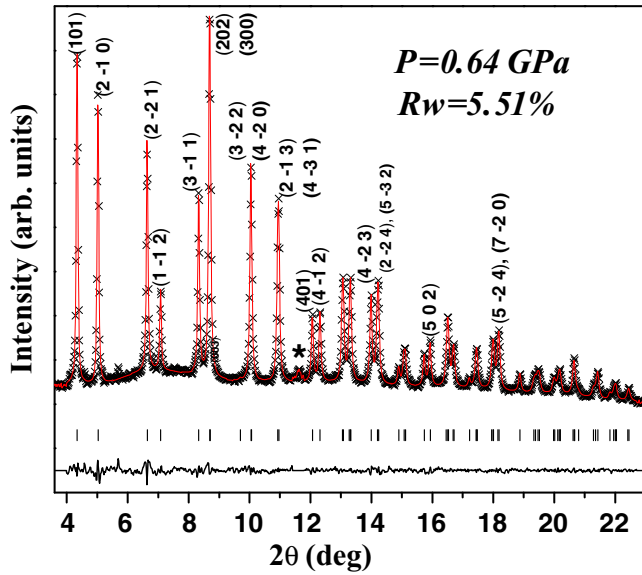
FIG. 6. (Color online) Rietveld refinement result at 0.64 GPa. The observed (crosses), calculated (solid line), and difference (bottom line) patterns are shown. The vertical bars show the peak positions for the refined hexagonal model. The symbol * indicates a peak from the steel gasket.

the refinement. The lattice change with pressure is shown in Fig. 7. The lattice is compressed at an almost constant rate in the entire pressure range, but the c direction is softer than the a direction. No anomalies are observed. The pressure dependent volume change can be seen in Fig. 8(b) (black triangles). A
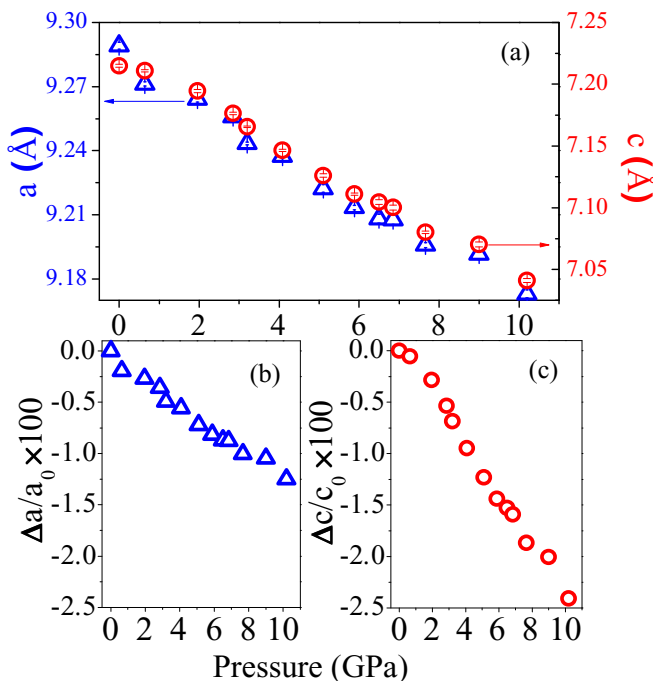
FIG. 7. (Color online) (a) Cell parameters of $HoAl_3(BO_3)_4$ obtained from the Rietveld refinements, with a (blue) and c (red) vs pressure shown, respectively. Pressure dependent percentage change in cell parameters, (b) a, (c) c, respectively.
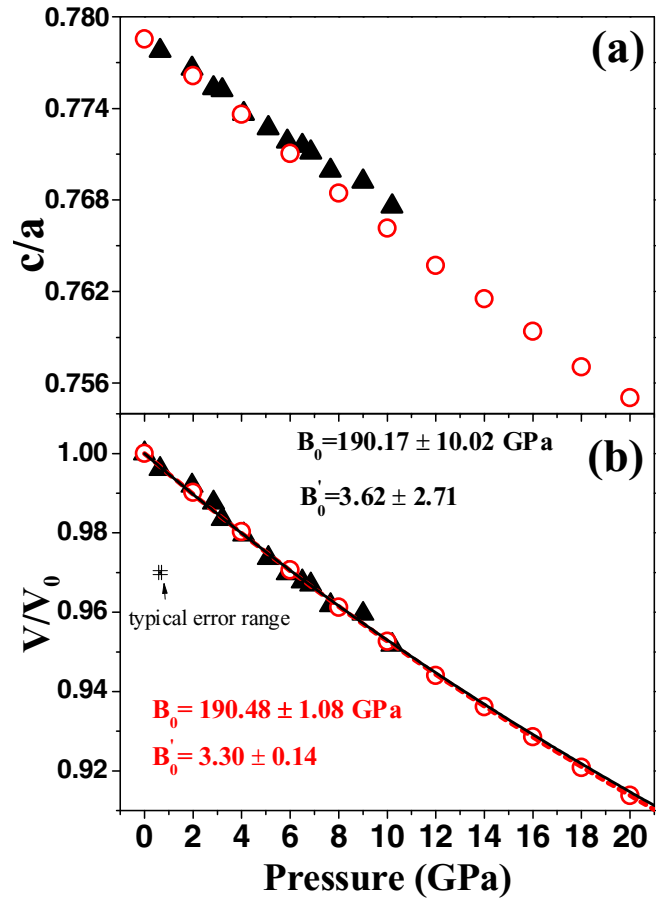

FIG. 8. (Color online) (a) Lattice parameter ratio c/a for experimental results (black triangles) and DFT calculated values (red circles). (b) V/V_0 for experimental results (black triangles) and DFT calculated values (red circles). The lines show the first order Murnaghan equation of state fit of experimental (solid) and DFT simulated (dash) results, respectively. $V_0 = 539.1 \, \text{Å}^3$ was used. Bulk Modulus (B_0, in GPa) compared with other materials, NaF (46.5), NaCl (24.0), MgO (156), $CaCO_3$ (75.27), 3C-SiC (248), and $LaMnO_3$ (108), indicates that this material is very stiff.

first order equation of state fit using the Murnaghan equation was performed, and the fitting curve is almost linear. The bulk modulus B_0 and its pressure derivative B_0' obtained from the fit are $B_0 = 190.93 \pm 10.35$ GPa, $B_0' = 3.30 \pm 2.75$ GPa. B_0' behaves normally (typical values of B_0' are between 2 to 8 [49]). No current data are available for B_0 for other materials in the RABO family. However, comparison can be made with the values of B_0 for some other well-known materials including (in GPa): NaCl (24.0), bulk silicon (94) [49], MgO (156), $CaCO_3$ (75.3), 3C-SiC (248) [50], diamond (442) [51], and $LaMnO_3$ (108) [52]. It can be seen that B_0 for $HoAl_3(BO_3)_4$ is close to 3C-SiC(248), indicating a very stiff material. This was also observed in these measurements as extreme difficulty in grinding this material.

DFT calculations were performed to make contact between models and the experiments. As can be seen in Fig. 8, the red closed circles are the DFT calculated results of c/a [Fig. 8(a)] and V/V_0 [Fig. 8(b)], respectively. The calculated values match reasonably well with the experimental results (black
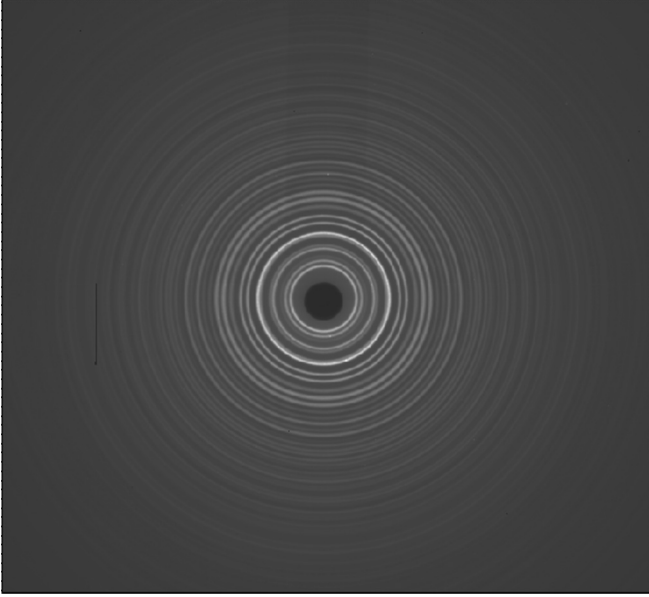
FIG. 9. Two-dimensional XRD raw data collected using a Perkin Elmer detector for the $HoAl_3(BO_3)_4$ powder sample. The data collected are very high quality with no bright spots from single crystal particles.

FIG. 10. (Color online) PDF $G(r)$ from the $HoAl_3(BO_3)_4$ powder sample (crosses), fit (red solid line), and the difference (bottom green line) are shown. The inset shows an expanded area of low r region with the corresponding bond(s) labeled.

triangles). Moreover, the bulk modulus B_0 obtained from DFT calculations has a value of $B_0 = 190.01$ GPa, which is almost the same as the refinement results. These results and the heat capacity results indicate that the system can be readily modeled with DFT methods. Our high pressure study also supports the observation of the anisotropic compressibility of $HoAl_3(BO_3)_4$, in which c is softer than a, as well as the stiffness of the sample. These properties should also be observed in temperature dependent experiments. The changes in structure coincide with the region of larger magnetoelectric effects at low temperature and may possibly be related. Since low temperature changes (lattice contraction) can be achieved by the application of high pressure, the application of pressure may enable us to probe low temperature properties and electrical polarization measurements under pressure should be explored.

D. High energy x-ray diffraction (PDF measurements)

High scattering angle XRD data on $HoAl_3(BO_3)_4$ powder samples were taken for a PDF study. The image for a typical data set can be seen in Fig. 9. Note that no high intensity spots from large single crystal particles are detected, and the circles are approximately continuous. The solid vertical line on the left side of the image shows a line of dead pixels in the detector, which was masked during data processing. Two independent data sets (A and B) were collected. The PDF technique is sensitive to the short-range structure and local bond distance in addition to the long-range periodic structure [40]. Local distortions can be readily determined. Figure 10 shows the refinement result of $HoAl_3(BO_3)_4$ from 1 to 20 Å at room temperature from set B. The first atomic pair distance is above 1 Å (see Table II), so the area between 0 and 1 Å was excluded from the refinement. The weighted R factor R_w
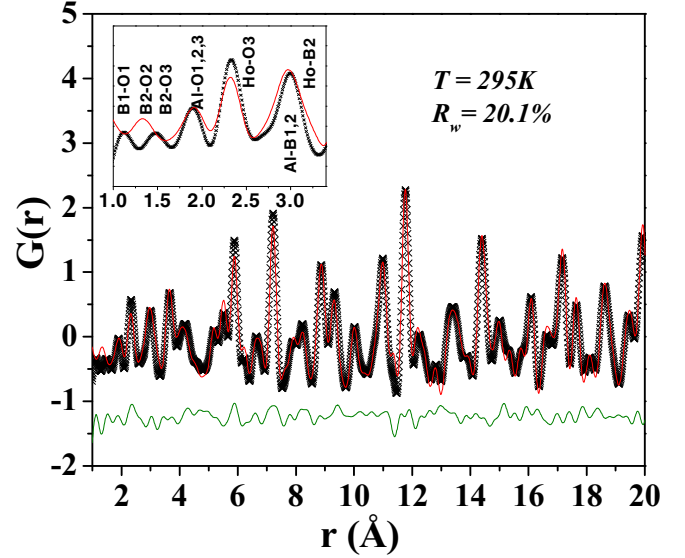
is 20.1%, which compares well with the value of perovskites such as $BaTiO_3$ [53] and other complex oxide systems. (Note that $R_w = \sqrt{\frac{\sum_{i=1}^{N} w(r_i)[G_{obs}(r_i) - G_{calc}(r_i)]^2}{\sum_{i=1}^{N} w(r_i)G_{obs}^2(r_i)}}$, with G_{obs} and G_{calc} as the experimental and calculated PDF, respectively, the weight for each data point is given by $w(r_i)$ [40].) ADPs ($U_{11} = U_{22} \neq U_{33}$) for Ho, Al, O1, O2, and O3 were refined, and U_{iso} was determined using $U_{iso} = (U_{11} + U_{22} + U_{33})/3$.

Figure 11 shows the temperature dependent lattice parameters retrieved from the PDF refinement. The result from set A matches well with the ones from set B, suggesting our
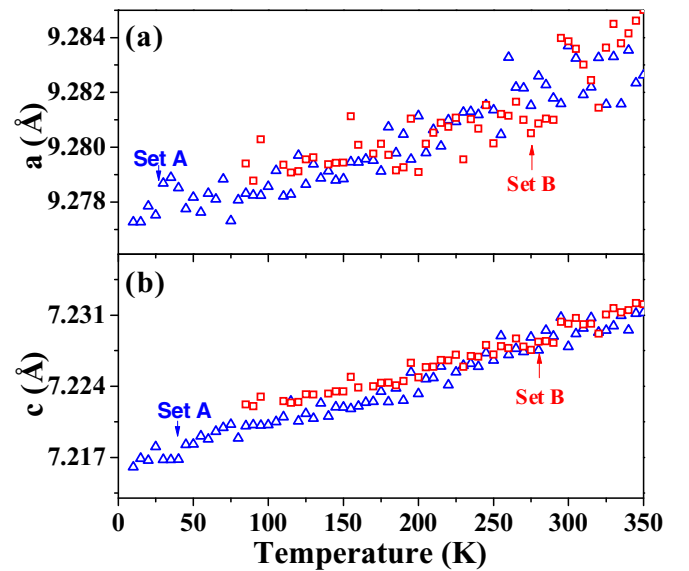

FIG. 11. (Color online) Cell parameters (a) a, (b) c, respectively, retrieved from fit of PDF $G(r)$. Blue triangles are the results from set A, while red squares are from set B.
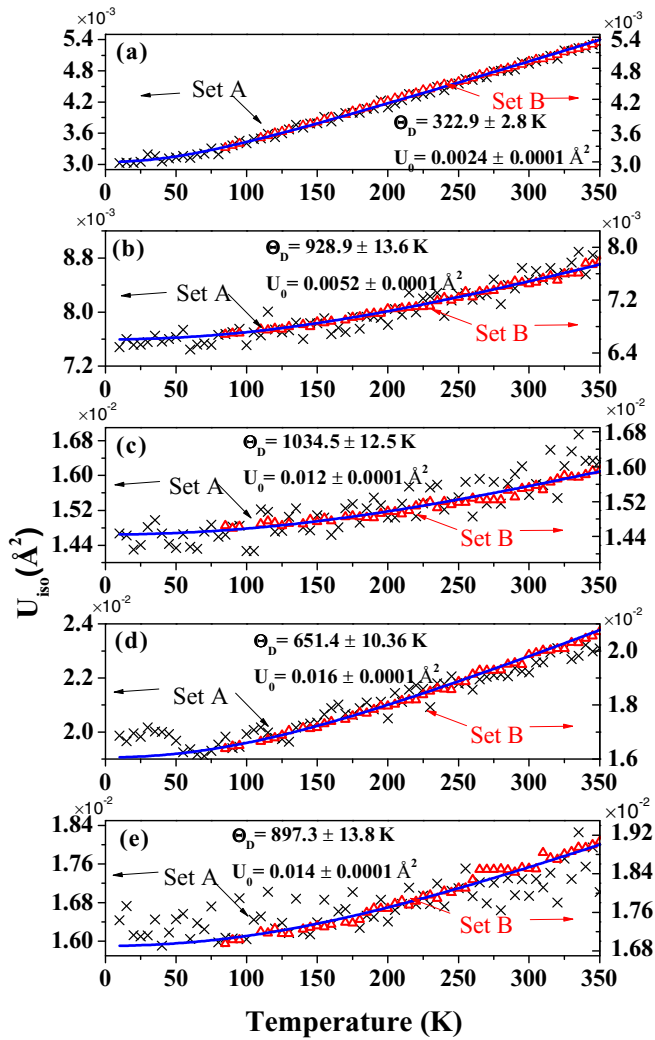
FIG. 12. (Color online) Refinement results of atomic displacement parameters (ADPs, U_{iso}) measured from 10 K to 350 K for each atom as (a) Ho, (b) Al, (c) O1 (d) O2, and (e) O3, respectively. Set A (crosses) and Set B (triangles) are plotted on the same graph. The blue solid lines stand for the Debye model fits for set B. A small bump is detected for Ho at about 30 K, and a very significant change is seen for O2 below 50 K.

results are very reproducible. It can be seen that the change of a in the whole temperature range is very small ($\sim 10^{-3}$ Å), while the change in c is relatively larger ($\sim 10^{-2}$ Å). This indicates that the cell is softer in the c direction, which agrees well with our observation from the pressure dependent XRD measurements. Temperature dependent ADPs are shown in Fig. 12 for (a) Ho, (b) Al, (c) O1, (d) O2, and (e) O3, respectively. The results from set A are more scattered than the results from set B, mainly due to the experimental setup difference (A has 60 s counting time while B has 240 s counting time per temperature point). However, the overall trends and average results are similar. The most unusual variation in the structural parameters of $HoAl_3(BO_3)_4$ occurs at low temperature; hence, set A is focused on. The blue curves in Fig. 12 are the fitting results based on a Debye model [54] given by $U = \frac{3h^2T}{4\pi^2 mk\theta^2}[\phi(x) + \frac{1}{4}x] + U_0$, where $x = \frac{\theta}{T}$
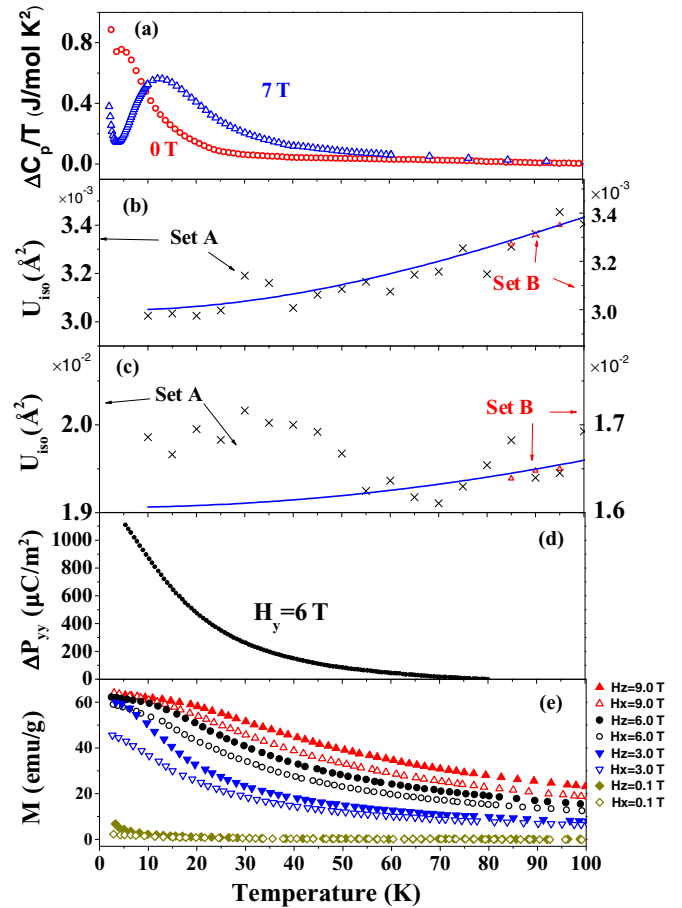

FIG. 13. (Color online) (a) Heat capacity measurements between 0 and 100 K at 0 T (red circles) and at 7 T (blue triangles), together with ADPs for (b) Ho, (c) O2, respectively. (d) Temperature and field dependences of magnetoelectric polarization ΔP_{yy} taken from Ref. [32]. (The magnetic field H was applied along the y axis, and the polarization was measured also along this axis.) (e) The reported magnetization data vs applied magnetic field (Ref. [32]). The solid symbols stand for $H_z = 9$ T (red), 6 T (black), 3 T (blue), and 0.1 T (dark yellow), respectively. The open symbols stand for $H_x = 9$ T (red), 6 T (black), 3 T (blue), and 0.1 T (dark yellow), respectively.

and $\phi(x) = \frac{1}{x} \int_0^x \frac{\xi d\xi}{e^\xi - 1}$; θ is the Debye temperature; h and k are the Planck and Boltzmann constants; m is the mass of the vibrating atom. U_0 reflects the static and nonthermal disorder. The U_0 parameter is quite small and is slightly modified by the experimental setup. Hence the data sets (A and B) are presented with slightly shifted scales (left scale and right scale, respectively) within the same window. It is noticed that the Debye temperatures determined from our fits for each atom are higher than typically found for the corresponding atoms [55]. For example, θ for a rare earth atom is usually <200 K, but here it is ~ 300 K. The value of θ for Al, O1, O2, and O are ~ 930, 1035, 651, and 897 K, respectively. It could be understood that because this is a very stiff material, the bonds for atoms should be stronger than those in a normal materials. The larger value of bulk modulus found in our high pressure XRD measurement also supports these results.

In further investigation of ADPs, a significant deviation is seen in U_{iso} of O2 below 50 K [Fig. 12(d)], as well as

FIG. 15. (Color online) Temperate dependent XAFS structure function indicating systematic reduction of all pair peaks with increased temperature.
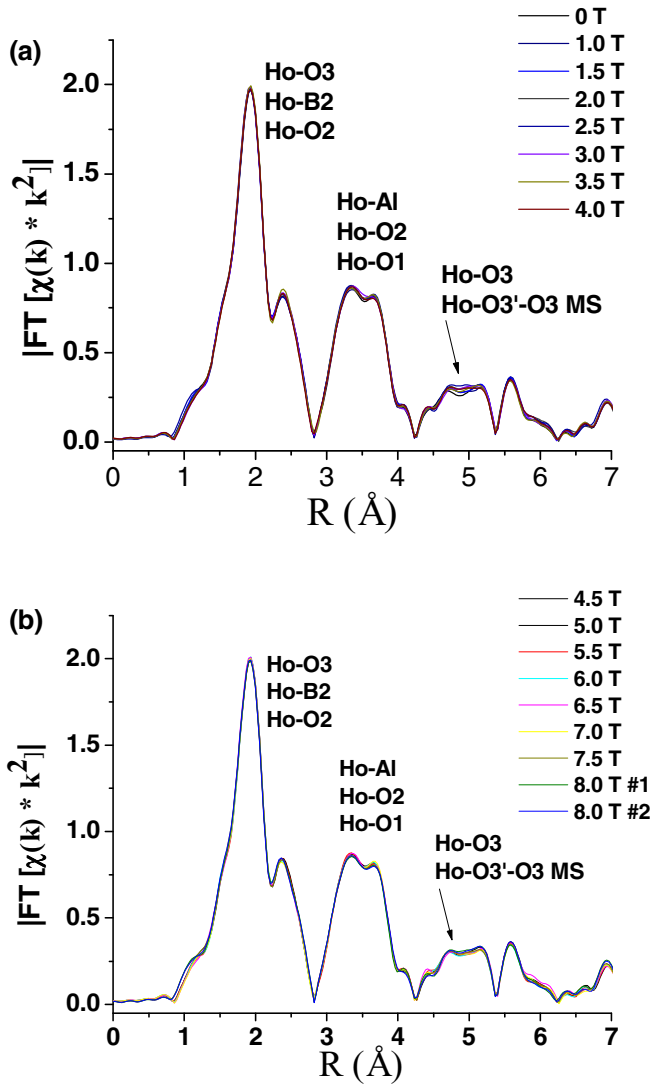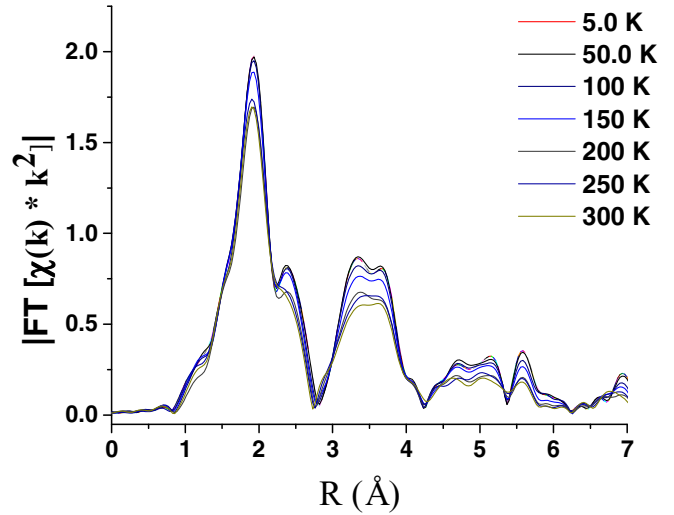

FIG. 14. (Color online) XAFS structure function (Fourier transform of fine structure times k^2) taken at 5 K for magnetic fields varying from 0 T to 4 T in (a) and 4.5 T to 8 T (b). Duplicate data sets at 8 T [in (b)] show the statistical variation in the data. Note that significant changes occur in the region near ∼5 Å with the largest change corresponding to magnetic fields increasing from 0 T to 3 T (the structural peaks are identified in Fig. 16).
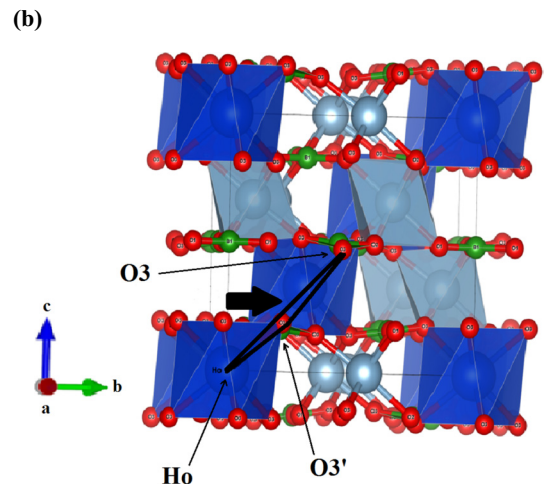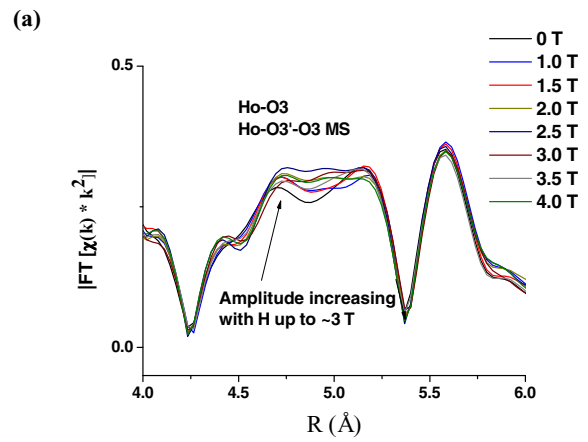

FIG. 16. (Color online) (a) Expanded XAFS structure functions for magnetic fields between 0 T and 4 T. (b) Single scattering path Ho-O3 and multiple scattering path (Ho-O3′-O3) associated with the peak. This strong variation at low field (0 to ∼3 T) is related enhanced coupling of neighboring HoO$_6$ polyhedra via the BO$_3$ planes.

suggestions of a jump in U_{iso} of Ho [Fig. 12(a)] at about 30 K. Such behavior of the refined ADPs is usually due to an overall inadequate structural model [56] or some short-ranged effect, which disagrees with the average long range structure. As we previously mentioned, no long range structural phase transition occurs in this temperature region. The system possibly exhibits a local distortion [57], in which the Ho and O2 atoms are involved. Figure 13 presents an expanded view of the data between 0 and 100 K. Figures 13(d) and 13(e) show the reported experimental data for electrical polarization and magnetization, taken from Ref. [32]. We note that the anomalies in the Ho and O2 ADPs occur in the temperature region where the large magnetoelectric effect in HoAl$_3$(BO$_3$)$_4$ can be seen. The combined results suggest that the local distortion inside the cell at low temperature may be relevant to
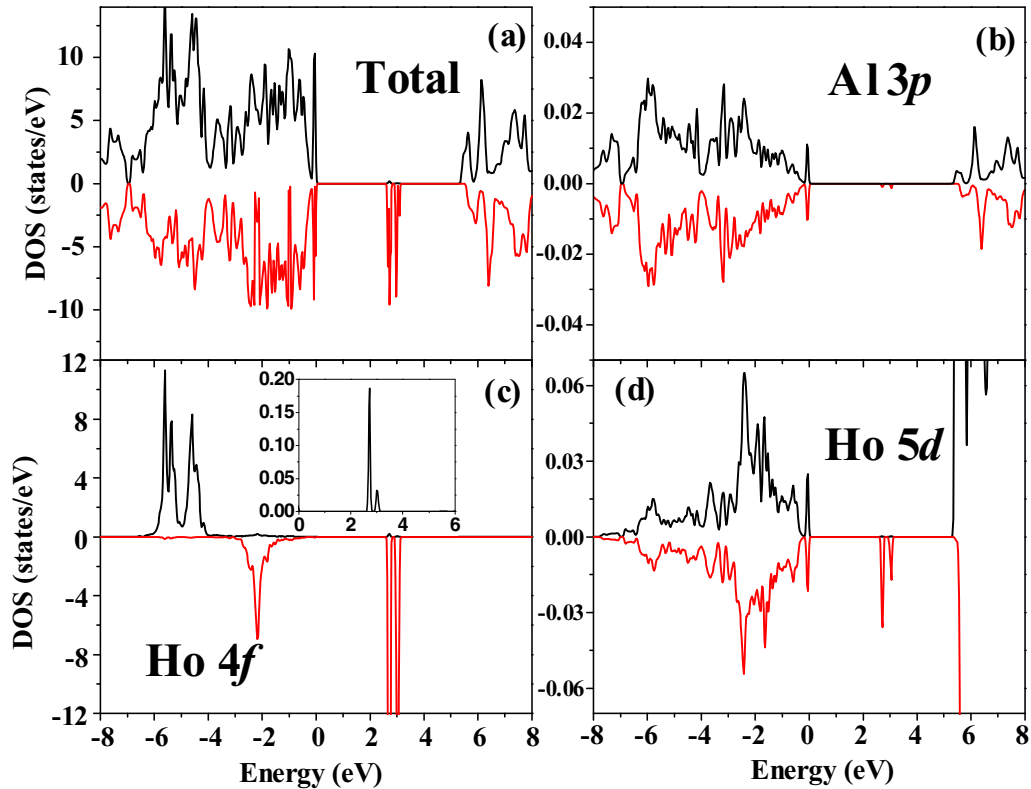
FIG. 17. (Color online) Total DOS (a) and the projected DOS of the Al-$3p$ (b), Ho-$4f$ (c), and Ho-$5d$ bands (d). The black lines stand for the spin up contributions, and red lines are for the spin down contributions. The inset in (c) is an expanded scale of the Ho $4f$ DOS between 0 and 6 eV.

the magnetoelectric effect of the system since the O2 atoms are outside the HoO_6 polyhedra. A picture of the structure beyond just the HoO_6 polyhedra under magnetic field is needed and will be addressed below.

E. XAFS measurements

Magnetic field dependent absorption measurements at a fixed temperature (5 K) are shown in Fig. 14, as the XAFS structure functions. Duplicate data sets at 8 T show the statistical variation in the data at fixed magnetic field. The most significant change in the structure with magnetic field occurs near ~ 5 Å. The structure changes significantly between 0 and 3 T and remains relatively stable for higher magnetic fields. The details will be described in depth below with the discussion of Fig. 16. Temperature dependent XAFS structure functions are presented in Fig. 15. The result indicates systematic reduction in all pair peaks with increased temperature. It is consistent with temperature variation of the lattice parameters (Fig. 11).

The peak mentioned in Fig. 14 with the most significant change with magnetic field is further examined in Fig. 16. It can be seen more clearly that the intensity of this peak near ~ 5 Å shows a strong variation with the magnetic fields up to ~ 3 T. This specific peak indicated by the arrow corresponds to scattering paths between Ho ions in one HoO_6 prism and the O3 atom on the nearby HoO_6 prism. A single scattering (Ho-O3) and a multiple scattering path (Ho-O3'-O3) that contribute to this peak are illustrated in Fig. 16(b). Meanwhile,

no significant variation with magnetic fields is found in the first peak, which corresponds to the nearest neighbor Ho-O3 shell in the HoO_6 polyhedra. Specifically, in Fig. 14, there is no significant change with magnetic fields in the nearest Ho-O3, Ho-B2, Ho-O2, and the next major shell containing Ho-Al and Ho-O1/O2 pairs. The data show that the HoO_6 polyhedra remain stable within the entire magnetic field range measured.

Recently, a microscopic model of $HoAl_3(BO_3)_4$ model was reported [32]. In the model, all Ho ions in the crystal hold equivalent positions and are surrounded by a slightly twisted O3 prism with a triangular base. The electron density distribution of the $4f$ subshell for a Ho^{3+} ion takes the form of an ellipsoid flattened along the quantization axis (along z). The model suggests that without an external magnetic field, the $4f$ subshell of a holmium ion takes the position that has the minimum overlap with the O3 shell, and the magnetic moment is directed along the z axis (half parallel and half antiparallel). When an external field is applied, for example, in the z direction, the magnetic moment of one half of the ions will rotate by 180°. During the rotation, the overlapping of electron (Ho $4f$ and the O3) charge density will arise, which will create additional electrostatic forces that will cause the strain in the lattice. Such strain will reach its maximum when the magnetic moment of Ho^{3+} is in the xy plane. During this process, the forces acting on the holmium ions will differ for different oxygen ions, and this will lead to a shift of a Ho^{3+} ion in the x direction. In the model, this process will eventually result in a decrease in the twist angle of the oxygen
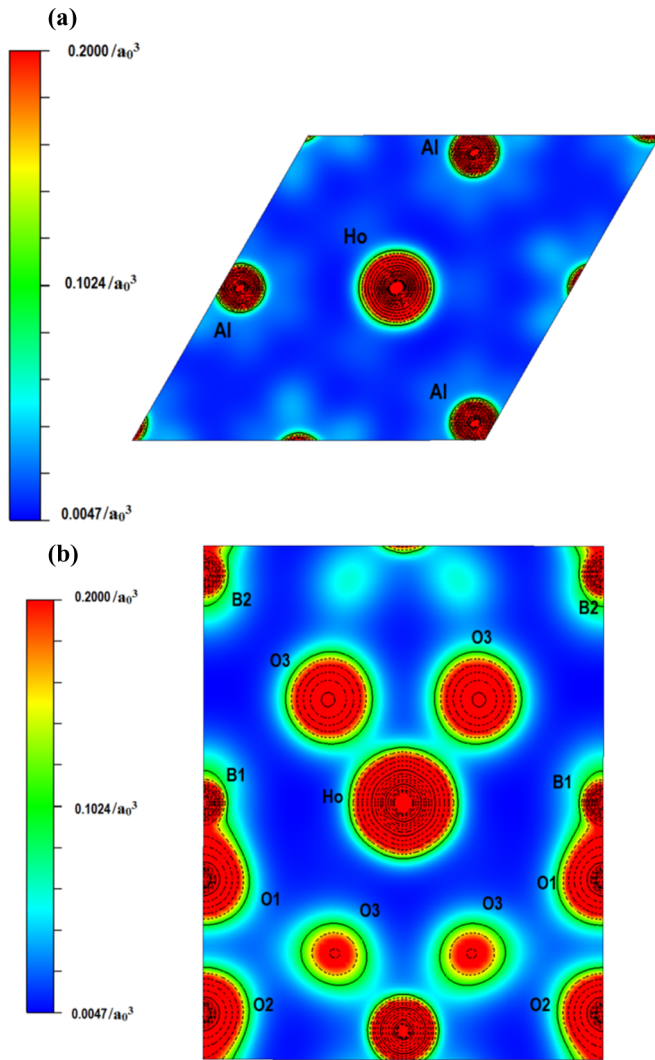
(a)

(b)

FIG. 18. (Color online) Cross section of the total electron density on (a) *ab* plane ($z = 0$) and (b) *ac* plane ($x = 0$). The Ho iron is centered in both images.
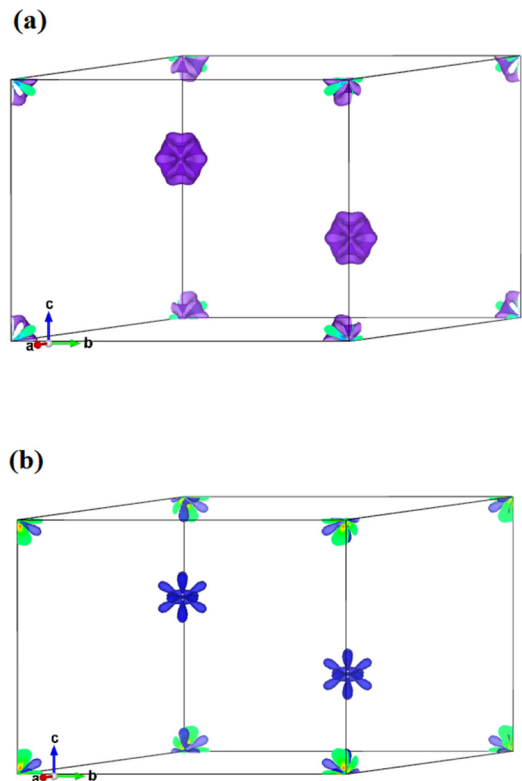
(a)

(b)

FIG. 19. (Color online) Spin density difference (spin up minus spin down) in three-dimensional space with the isosurface level equal to (a) $0.02/a_0^3$ and (b) $-0.02/a_0^3$, respectively. This emphasizes the Ho $4f$ band. Only the Ho site has nonzero spin density difference.

prism, and thus an electric dipole arises. This model agrees well with the observed fact in Ref. [31] that the $HoAl_3(BO_3)_4$ crystal undergoes positive magnetostriction λ_x and reaches its maximum at about 3 T; however, it continues to drop with the increasing magnetic field because according to the model, the strain caused by the rotation of magnetic moment of Ho^{3+} will reach its maximum when it has rotated by $90°$, after which it will continue to drop.

With respect to the XAFS results in magnetic field, we note that the absence of changes in Ho-O3 nearest neighbor peak is inconsistent with the proposed theoretical model (Ref. [32]). Meanwhile, the strong variation of the Ho-O3 and Ho-O3'-O3 peaks reflects the fact that coupling between two nearby HoO_6 polyhedra will be enhanced with increased magnetic field up to ∼3 T, reach its maximum, and maintain the level between 3 to 8 T. In this system, the magnetic field couples to the lattice and rotates the HoO_6 polyhedra initially, but the stiffness of the lattice prevents rotations beyond a certain range. Hence, increasing the field has no effect beyond a cut-off magnetic field (∼3 T in this case).

F. DFT calculation

Our calculated LSDA + U DOS is shown in Fig. 17; the total DOS reveals a wide bandgap of HABO with the value of ∼5 eV, with localized $4f$ states in the middle of the gap. These results are consistent with the DFT calculations on $TbAl_3(BO_3)_4$ [30]. The spin up states of Ho $4f$ are mostly between -6 and -3 eV, while the spin down states have a peak at about -2 eV and also occur near the center of the gap. The peak near -2 eV for the $4f$ spin down DOS is found in other rare earth borate systems, including $TbFe_3(BO_3)_4$ [58] and $TbAl_3(BO_3)_4$. But in the Ho system, it is much broader. Unlike the iron borates, only the R ion (Ho for example) contributes to the magnetic properties. Specifically, Al [Fig. 17(b)] and oxygen (not shown) shows no direct or induced magnetization based on the calculated DOS.

The total electron density with spin up + spin down is plotted in Fig. 18. The projection on the *ab* and *ac* planes reveals that the Ho charge distribution is a very slightly distorted sphere. In order to study the Ho $4f$ contribution to the total electron density and its spatial distribution, we calculated the spin density difference (spin up – spin down) [59] (see Fig. 19). It is seen that the magnetic contribution comes from the Ho site only. The negative isosurfaces [for occupied $4f$ states near ∼-2 eV shown in Fig. 17(c)] take the shape of multiple lobes [Fig. 19(b)], and the positive ones (for states between -6 and -3 eV) have the shape shown in Fig. 19(a). All isosurfaces have a high symmetry and are not significantly distorted with respect to any particular direction. In other

words, to first order, this moment can be rotated under external magnetic field. Therefore, it is unlikely that the rotation of Ho $4f$ moments will cause significant strain inside the HoO_6 polyhedra. This result supports our results derived from the XAFS measurement that the magnetoelectric properties of HABO system should not be related to the distortion inside the HoO_6 prism.

IV. SUMMARY

The magnetostructural properties of $HoAl_3(BO_3)_4$ were explored by temperature and magnetic field dependent heat capacity measurements, pressure and temperature dependent x-ray diffraction measurements, as well as temperature and magnetic field dependent XAFS measurements. The heat capacity was measured (from 2 to 300 K) in magnetic fields (from 0 to 7 T), and the structure was measured from ∼10 to 350 K. The structure for isotropic pressures between ambient and 10.2 GPa was also measured. Local structural measurements were conducted in magnetic fields (between 0 and 8 T at 5 K). These measurement results were combined with density functional calculations to predict the lattice contribution to the heat capacity, the pressure dependent structure, the electronic structure, and the spin decomposed charge density. An anomalous change in the structure is found in the region of large magnetoelectric effects, which may be related. More detailed high-resolution temperature dependent structural measurements and combined magnetic field and temperature structural studies are needed to provide a link between the ground state structure and the magnetoelectric effects.

From a local structure perspective, no significant change or distortion of the HoO_6 polyhedra is seen to occur with magnetic field. However, the magnetic field dependent structural measurements reveal enhanced correlation between neighboring HoO_6 polyhedra. This observed response is seen to saturate approximately between 2 and 3 T due to the lattice stiffness. These results provide a microscopic level understanding of the mechanism behind the large electric polarization induced by magnetic fields in the general class of $RAl_3(BO_3)_4$ systems (R = rare earth).

[1] H. Wu, L. Li, L.-Z. Liang, S. Liang, Y.-Y. Zhu, and X.-H. Zhu, J. Eur. Ceram. Soc. **35**, 411 (2015); R. D. Johnson and P. G. Radaelli, Annu. Rev. Mater. Res. **44**, 269 (2014); N. A. Spaldin, S. W. Cheong, and R. Ramesh, Phys. Today **63**, 38 (2010); K. F. Wang, J. M. Liu, and Z. F. Ren, Adv. Phys. **58**, 321 (2009); R. Ramesh and N. A. Spaldin, Nat. Mater. **6**, 21 (2007); S.-W. Cheong and M. Mostovoy, *ibid.* **6**, 13 (2007).

[2] J. Van Den Brink and D. I. Khomskii, J. Phys.: Condens. Matter **20**, 434217 (2008).

[3] B. D. Stojanovic, C. Jovalekic, V. Vukotic, A. Z. Simoes, and J. A. Varela, Ferroelectrics **319**, 65 (2005).

[4] M. Vopsaroiu, M. G. Cain, G. Sreenivasulu, G. Srinivasan, and A. M. Balbashov, Mater. Lett. **66**, 282 (2012).

[5] A. Roy, R. Gupta, and A. Garg, Adv. Condens. Matter Phys. **2012**, 1 (2012); M. M. Vopson, E. Zemaityte, M. Spreitzer, and E. Namvar, J. Appl. Phys. **116**, 113910 (2014); J. F. Scott, Nat. Mater. **6**, 256 (2007); M. Gajek, M. Bibes, S. Fusil, K. Bouzehouane, J. Fontcuberta, A. Barthélémy, and A. Fert, *ibid.* **6**, 296 (2007).

[6] Y. Chye, T. Liu, D. Li, K. Lee, D. Lederman, and T. H. Myers, Appl. Phys. Lett. **88**, 132903 (2006).

[7] L. Kozielski and F. Clemens, Proc. Appl. Ceramics **6**, 15 (2012).

[8] G. Lawes, A. Harris, T. Kimura, N. Rogado, R. Cava, A. Aharony, O. Entin-Wohlman, T. Yildirim, M. Kenzelmann, C. Broholm, and A. Ramirez, Phys. Rev. Lett. **95**, 087205 (2005).

[9] A. Arkenbout, T. Palstra, T. Siegrist, and T. Kimura, Phys. Rev. B **74**, 184431 (2006).

[10] S. Park, Y. Choi, C. Zhang, and S. W. Cheong, Phys. Rev. Lett. **98**, 057601 (2007).

[11] T. Kimura, J. C. Lashley, and A. P. Ramirez, Phys. Rev. B **73**, 220401(R) (2006).

[12] Y. Yamasaki, S. Miyasaka, Y. Kaneko, J. P. He, T. Arima, and Y. Tokura, Phys. Rev. Lett. **96**, 207204 (2006).

[13] X. K. Wei, T. Zou, F. Wang, Q. H. Zhang, Y. Sun, L. Gu, A. Hirata, M. W. Chen, Y. Yao, C. Q. Jin, and R. C. Yu, J. Appl. Phys. **111**, 073904 (2012).

[14] J. Hwang, E. S. Choi, H. D. Zhou, J. Lu, and P. Schlottmann, Phys. Rev. B **85**, 024415 (2012).

[15] M. Shang, C. Zhang, T. Zhang, L. Yuan, L. Ge, H. Yuan, and S. Feng, Appl. Phys. Lett. **102**, 062903 (2013); X. Xu and W. Wang, Mod. Phys. Lett. B **28**, 1430008 (2014).

[16] F. Hong, Z. Cheng, and X. Wang, J. Appl. Phys. **112**, 013920 (2012); J. Magesh, P. Murugavel, R. V. K. Mangalam, K. Singh, C. Simon, and W. Prellier, *ibid.* **112**, 104116 (2012); B. Lorenz, ISRN Condens. Matter Phys. **2013**, 1 (2013); T. Kimura, T. Goto, H. Shintani, K. Ishizaka, T. Arima, and Y. Tokura, Nature **426**, 55 (2003); N. Hur, S. Park, P. A. Sharma, S. Guha, and S. W. Cheong, Phys. Rev. Lett. **93**, 107207 (2004).

[17] O. Zaharko and H. Berger, J. Phys.: Condens. Matter **22**, 056002 (2010); F. Wu, E. Kan, C. Tian, and M. H. Whangbo, Inorg. Chem. **49**, 7545 (2010); Y. S. Oh, S. Artyukhin, J. J. Yang, V. Zapf, J. W. Kim, D. Vanderbilt, and S. W. Cheong, Nat. Commun. **5**, 3201 (2014).

[18] N. Ikeda, H. Ohsumi, K. Ohwada, K. Ishii, T. Inami, K. Kakurai, Y. Murakami, K. Yoshii, S. Mori, Y. Horibe, and H. Kitô,

Nature **436**, 1136 (2005); M. A. Subramanian, T. He, J. Chen, N. S. Rogado, T. G. Calvarese, and A. W. Sleight, Adv. Mater. **18**, 1737 (2006).

[19] K. C. Liang, W. Zhang, B. Lorenz, Y. Y. Sun, P. S. Halasyamani, and C. W. Chu, Phys. Rev. B **86**, 094414 (2012).

[20] A. K. Zvezdin, S. S. Krotov, A. M. Kadomtseva, G. P. Vorob'ev, Y. F. Popov, A. P. Pyatakov, L. N. Bezmaternykh, and E. A. Popova, JETP Lett. **81**, 272 (2005); F. Yen, B. Lorenz, Y. Sun, C. Chu, L. Bezmaternykh, and A. Vasiliev, Phys. Rev. B **73**, 054435 (2006); S. S. Krotov, A. M. Kadomtseva, Y. F. Popov, G. P. Vorob'ev, A. V. Kuvardin, K. I. Kamilov, L. N. Bezmaternykh, and E. A. Popova, J. Magn. Magn. Mater. **300**, e426 (2006); Ph. Goldner, O. Guillot-Noël, J. Petit, M. Popova, and L. Bezmaternykh, Phys. Rev. B **76**, 165102 (2007); T. Kurumaji, K. Ohgushi, and Y. Tokura, *ibid.* **89**, 195126 (2014).

[21] T. N. Stanislavchuk, E. P. Chukalina, M. N. Popova, L. N. Bezmaternykh, and I. A. Gudim, Phys. Lett. A **368**, 408 (2007).

[22] R. Chaudhury, F. Yen, B. Lorenz, Y. Sun, L. Bezmaternykh, V. Temerov, and C. Chu, Phys. Rev. B **80**, 104424 (2009); C. Ritter, A. Vorotynov, A. Pankrats, G. Petrakovskii, V. Temerov, I. Gudim, and R. Szymczak, J. Phys.: Condens. Matter **20**, 365209 (2008); A. Pankrats, G. Petrakovskii, A. Kartashev, E. Eremin, and V. Temerov, *ibid.* **21**, 436001 (2009); A. A. Demidov and D. V. Volkov, Phys. Solid State **53**, 985 (2011); V. I. Zinenko, M. S. Pavlovskii, A. S. Krylov, I. A. Gudim, and E. V. Eremin, J. Exp. Theor. Phys. **117**, 1032 (2014); D. K. Shukla, S. Francoual, A. Skaugen, M. v. Zimmermann, H. C. Walker, L. N. Bezmaternykh, I. A. Gudim, V. L. Temerov, and J. Strempfer, Phys. Rev. B **86**, 224421 (2012).

[23] J. E. Hamann-Borrero, S. Partzsch, S. Valencia, C. Mazzoli, J. Herrero-Martin, R. Feyerherm, E. Dudzik, C. Hess, A. Vasiliev, L. Bezmaternykh, B. Büchner, and J. Geck, Phys. Rev. Lett. **109**, 267202 (2012).

[24] K. N. Boldyrev, T. N. Stanislavchuk, A. A. Sirenko, L. N. Bezmaternykh, and M. N. Popova, Phys. Rev. B **90**, 121101 (2014).

[25] K. N. Boldyrev, T. N. Stanislavchuk, S. A. Klimin, M. N. Popova, and L. N. Bezmaternykh, Phys. Lett. A **376**, 2562 (2012).

[26] K. N. Boldyrev and D. A. Erofeev, Opt. Spectrosc. **116**, 872 (2014).

[27] E. A. Popova, A. N. Vasiliev, V. L. Temerov, L. N. Bezmater-nykh, N. Tristan, R. Klingelerm, and B. Büchner, J. Phys.: Condens. Matter **22**, 116006 (2010).

[28] E. A. Popova, D. V. Volkov, A. N. Vasiliev, A. A. Demidov, N. P. Kolmakova, I. A. Gudim, L. N. Bezmaternykh, N. Tristan, Yu. Skourski, B. Büchner, C. Hess, and R. Klingeler, Phys. Rev. B **75**, 224413 (2007).

[29] R. P. Chaudhury, B. Lorenz, Y. Y. Sun, L. N. Bezmaternykh, V. L. Temerov, and C. W. Chu, Phys. Rev. B **81**, 220402(R) (2010).

[30] Y. Saeed, N. Singh, and U. Schwingenschlögl, J. Appl. Phys. **110**, 103512 (2011).

[31] K. C. Liang, R. P. Chaudhury, B. Lorenz, Y. Y. Sun, L. N. Bezmaternykh, V. L. Temerov, and C. W. Chu, Phys. Rev. B **83**, 180417(R) (2011).

[32] A. L. Freydman, A. D. Balaev, A. A. Dubrovskiy, E. V. Eremin, V. L. Temerov, and I. A. Gudim, J. Appl. Phys. **115**, 174103 (2014).

[33] L. N. Bezmaternykh, V. L. Temerov, I. A. Gudim, and N. A. Stolbovaya, Crystallogr. Rep. **50**, S97 (2005).

[34] H. Chen, T. Yu, P. Gao, J. Bai, J. Tao, T. A. Tyson, L. Wang, and R. Lalancette, Inorg. Chem. **52**, 9692 (2013).

[35] J. S. Hwang, K. J. Lin, and C. Tien, Rev. Sci. Instrum. **68**, 94 (1997).

[36] P. Blaha, K. Schwarz, G. Madsen, D. Kvasnicka, and J. Luitz, *An augmented plane wave+ local orbitals program for calculating crystal properties* (Vienna University of Technology, Vienna, Austria, 2001).

[37] J. Hafner, J. Comp. Chem. **29**, 2044 (2008); G. Kresse and J. Furthmüller, Comput. Mat. Sci. **6**, 15 (1996); Phys. Rev. B **54**, 11169 (1996).

[38] A. Hammersley, European Synchrotron Radiation Facility Internal Report ESRF97HA02T (1997).

[39] V. Petricek, M. Dusek, and L. Palatinus, Z. Kristallogr. **229**, 345 (2014).

[40] R. B. Neder and T. Proffen, *Diffuse Scattering and Defect Structure Simulations* (Oxford University Press, Oxford, 2008); T. Egami and S. L. J. Billinge, *Underneath the Bragg Peaks: Structural Analysis of Complex Materials* (Pergamon, Amsterdam, 2003); T. Proffen, S. J. L. Billinge, T. Egami, and D. Louca, Z. Kristallogr. **218**, 132 (2003); V. Petkov, *Characterization of Materials* (Wiley, Hoboken, NJ, 2012).

[41] P. Juhas, T. Davis, C. L. Farrow, and S. J. Billinge, J. Appl. Crystallogr. **46**, 560 (2013).

[42] C. Farrow, P. Juhas, J. Liu, D. Bryndin, E. Božin, J. Bloch, T. Proffen, and S. Billinge, J. Phys.: Condens. Matter **19**, 335219 (2007).

[43] J. Lu, C. Fu, and J. Chen, Appl. Opt. **50**, 116 (2011).

[44] A. I. Begunov, A. A. Demidov, I. A. Gudim, and E. V. Eremin, JETP Lett. **97**, 528 (2013).

[45] M. Janoschek, P. Fischer, J. Schefer, B. Roessli, V. Pomjakushin, M. Meven, V. Petricek, G. Petrakovskii, and L. Bezmaternikh, Phys. Rev. B **81**, 094429 (2010); P. Fischer, V. Pomjakushin, D. Sheptyakov, L. Keller, M. Janoschek, B. Roessli, J. Schefer, G. Petrakovskii, L. Bezmaternikh, V. Temerov, and D. Velikanov, J. Phys. Condens. Matter **18**, 7975. (2006).

[46] C. Ritter, A. Pankrats, I. Gudim, and A. Vorotynov, J. Phys. Condens. Matter **24**, 386002 (2012).

[47] C. Ritter, A. Vorotynov, A. Pankrats, G. Petrakovskii, V. Temerov, I. Gudim, and R. Szymczak, J. Phys. Condens. Matter **22**, 206002 (2010); C. Ritter, A. Balaev, A. Vorotynov, G. Petrakovskii, D. Velikanov, V. Temerov, and I. Gudim, *ibid.* **19**, 196227 (2007).

[48] T. Heitmann, Q. Zhang, K. C. Liang, L. M. Bezmaternykh, V. L. Temerov, B. Lorenz, and D. Vaknin, Annual Fall Meeting of the APS Prairie Section, PSF13 Meeting of the American Physical Society (2013). MWS_PSF13-2013-000081; T. Heitmann (private communications).

[49] V. G. Tyuterev and N. Vast, Comput. Mater. Sci. **38**, 350 (2006).

[50] K. Strössner, M. Cardona, and W. J. Choyke, Solid State Commun. **63**, 113 (1987).

[51] M. L. Cohen, Phys. Rev. B **32**, 7988 (1985).

[52] I. Loa, P. Adler, A. Grzechnik, K. Syassen, U. Schwarz, M. Hanfland, G. Kh. Rozenberg, P. Gorodetsky, and M. P. Pasternak, Phys. Rev. Lett. **87**, 125501 (2001).

[53] M. B. Smith, K. Page, T. Siegrist, P. L. Redmond, E. C. Walter, R. Seshadri, L. E. Brus, and M. L. Steigerwald, J. Am. Chem. Soc. **130**, 6955 (2008); V. Petkov, M. Gateshki, M. Niederberger, and Y. Ren, Chem. Mater. **18**, 814 (2006).

[54] P. Debye, Ann. Phys. (Berlin, Germany) **344**, 789 (1912).

[55] D. R. Chipman, J. Appl. Phys. **31**, 2012 (1960); M. Rosen, Phys. Rev. Lett. **19**, 695 (1967); R. N. Clayton, and S. W. Kieffer, Geochem. Soc. **3**, 3 (1991); R. Gumeniuk, W. Schnelle, H. Rosner, M. Nicklas, A. Leithe-Jasper, and Y. Grin, Phys. Rev. Lett. **100**, 017002 (2008).

[56] K. R. Knox, E. S. Bozin, C. D. Malliakas, M. G. Kanatzidis, and S. J. L. Billinge, Phys. Rev. B **89**, 014102 (2014).

[57] K. R. Knox, A. M. M. Abeykoon, H. Zheng, W.-G. Yin, A. M. Tsvelik, J. F. Mitchell, S. J. L. Billinge, and E. S. Bozin, Phys. Rev. B **88**, 174114 (2013).

[58] C. Lee, J. Kang, K. H. Lee, and M. H. Whangbo, Chem. Mater. **21**, 2534 (2009).

[59] M. Gamża, A. Ślebarski, and H. Rosner, EPJ B **67**, 483 (2009); S. Goumri-Said and M. B. Kanoun, J. Phys. D: Appl. Phys. **41**, 035004 (2008).